Energy Deposition and Characterization of Single-Event Upset and Latch-Up Cross Sections With 14 MeV and Thermal Neutrons

Matteo Cecchetto, Rubén García Alía, *Member, IEEE*, Giuseppe Lerner, Kacper Bilko, Francesc Salvat Pujol, Vasilis Vlachoudis, and Francesco Cerutti

***Abstract*— Single-event latch-up (SEL) cross sections of static random access memory (SRAM) at high energy (100–200 MeV) are generally not reproducible with 14-MeV neutrons, differently to single-event upset (SEU) cross sections. We explain this phenomenon through Monte Carlo simulations, analyzing neutron–silicon interactions and the indirect energy deposition in sensitive volumes (SVs) resembling the two mechanisms, showing that the former approach is not sufficient to explain how the energy is deposited. The SRAMs were characterized in monoenergetic and spallation facilities and their Monte Carlo model was validated using various particle beams. Additionally, the contribution of individual ions to the SEU and SEL cross sections is quantified, demonstrating the distinct impact of these ions in the two mechanisms. For instance, alpha particles play a significant role in triggering SEUs, while they hardly induce SELs. This is related to the energy released by the ion in correlation with its range and the size of the SV. Finally, the models are validated against thermal neutrons, and the SEL sensitivity is also investigated, demonstrating the absence of SEL for devices with a linear energy transfer (LET) threshold above 2 MeV $\cdot$ cm^2/mg.**

***Index Terms*— Commercial-off-the-shelf (COTS), energy deposition, fluktuierende kaskade (FLUKA), Geant4-based single event effect (G4SEE), linear energy transfer (LET), Monte Carlo simulations, neutrons, rectangular parallelepiped (RPP) models, single-event effect (SEE), single-event latch-up (SEL), single-event upset (SEU), static random access memory (SRAM).**

I. Introduction

SINGLE-EVENT upsets (SEUs) and single-event latch-ups (SELs) pose significant challenges for electronics in the large hadron collider (LHC) at CERN and also in space, atmospheric, fusion, automotive, and high-reliability ground-level applications. These environments, except for space, are mainly characterized by neutron fluxes with energies ranging over several orders of magnitude. Typically, commercial-off-the-shelf (COTS) components are employed in these environments, due to the large number of devices involved, performance, and lower costs with respect to radiation-hardened electronics. However, the response of COTS to radiation is typically not known, as the manufacturer rarely provides such information, and hence, electronics testing is needed and performed in dedicated facilities. The JEDEC JESD89B standard [1] and findings in [2] and [3] provide some neutron testing guidelines for electronics to operate in ground-level and accelerator environments, respectively. A spallation neutron source provides the closest spectrum to the terrestrial neutron environment; however, access to such facilities is limited in the world. In addition, as the SEU and SEL cross sections measured in such facilities encompass the information of a broad neutron energy spectrum in a single value, the response of a device as a function of the energy cannot be extracted. As a consequence, the suggested approach [1] to characterize electronics relies on monoenergetic measurements with at least four different energies: protons at 200, 100, and 50 MeV and neutrons at 14 MeV. Indeed, above 50 MeV, the neutron and proton SEU cross sections are equivalent according to the JEDEC standard [1], and regarding accelerator applications, the typical approximation is to set the limit at 20 MeV [4], [5], [6], [7]. The equivalence of neutron- and proton-induced SEU cross sections above a few tens of MeV is also shown in [7] and for high energies in [8] and [9]. Hence, testing above 20 MeV is more feasible with protons due to the impossibility of producing monoenergetic neutrons at such high energies without the presence of a secondary low-energy component (quasi-monoenergetic neutrons), which would complicate the analysis [9]. The final single-event effect (SEE) response is determined by fitting the cross section measurements with a Weibull function, offering the advantage of calculating the SEE rate for every environment (given its spectrum).

On the other hand, SEU and SEL cross sections of static random access memory (SRAM) do not exhibit the same energy dependence, as detailed in Section III, with SEL responses generally manifesting an onset around 20 MeV and an asymptotic response at high energy above 150–200 MeV [10], while SEU cross sections have already reached their maximum above 20 MeV, with similar values at 14 MeV. This observation is valid for the SRAM tested in this study as well as for several others reported in the literature. While these results can be considered representative of typical responses, it is important to note that variations in response may occur in other SRAMs, for instance, due to differences in design, process technology,

Received 20 December 2024; accepted 14 January 2025. Date of publication 5 March 2025; date of current version 18 August 2025. This work was supported by the European Union's Horizon 2020 Research and Innovation Program, corresponding to the Radiation Facility Network for the Exploration of Effects for Industry and Research (RADNEXT) Project, under Grant 101008126. *(Corresponding author: Matteo Cecchetto.)*

The authors are with CERN, CH-1211 Geneva, Switzerland (e-mail: matteo.cecchetto@cern.ch).

Color versions of one or more figures in this article are available at https://doi.org/10.1109/TNS.2025.3548299.

Digital Object Identifier 10.1109/TNS.2025.3548299

© 2025 The Authors. This work is licensed under a Creative Commons Attribution 4.0 License.
For more information, see https://creativecommons.org/licenses/by/4.0/

presence of high-Z materials, and operational conditions. Notably, the asymptotic cross section will be denoted as a high-energy cross section (σ_{HE}) throughout this article, which is also called cross section in saturation in other publications.

In addition, 14-MeV neutrons were shown to provide a reliable SEU cross section for SRAMs (<250 nm) and SRAM-based field programmable gate array (FPGA) to operate in atmospheric environments, with respect to using a spallation source, although multiple cell upsets (MCUs) are typically underestimated [11]. Similarly, 14-MeV neutrons provided compatible SEU cross sections, even though with some underestimations, to 230-MeV protons, employed to characterize the high-energy response for accelerator applications [5]. Therefore, 14-MeV neutron generators are an important resource for testing against SEUs, as they are typically more available and cost-efficient with respect to spallation or high-energy cyclotrons.

However, 14-MeV neutrons have been shown to significantly underestimate the SEL cross sections by more than two orders of magnitude with respect to high-energy protons [5]. This article aims to clearly explain the reason behind this difference, specifically why SEL cross sections are typically not reproducible with 14-MeV neutrons as opposed to the SEU cross sections. The evaluation is performed through fluktuierende kaskade (FLUKA) Monte Carlo simulations [12], [13], [14], [15], by studying the neutron–silicon interactions and the energy deposited in SEU and SEL models representative of actual SRAM memories, which were experimentally tested. The contribution of the single produced ions to the SEE cross sections is simulated through Geant4-based single event effect (G4SEE), a Geant4-based tool [16]. Moreover, the SEU and SEL analyses through the energy deposition are also performed considering thermal neutrons, which are known to induce SEUs in the accelerator [2], atmospheric [17], and fusion environments [18] but are not responsible for SELs.

II. Test Facilities and Setups

The SEE cross sections were measured with high-energy protons produced by cyclotrons either at the Proton Irradiation Facility (PIF) at the Paul Scherrer Institute (PSI) in Switzerland [19] or at the Kernfysisch Versneller Instituut (KVI) facility in The Netherlands [20]. The 14-MeV cross sections were measured either at the generator of neutrons for science and irradiations (GENEPI2) at LPSC in France [21] or at the Frascati neutron generator (FNG) in Italy [22], both producing neutrons through the interaction of a deuteron beam with a tritium target. Moreover, the atmospheric neutron cross sections were measured at the chip irradiation (ChipIr) spallation facility in the U.K. [23], and at the TRIUMF-BL1B facility in Canada [24], which provide atmospheric-like neutrons produced by 700- and 480-MeV protons impacting a tungsten target, respectively. Data from these already-published tests will be cited, while the TRIUMF beam time was awarded through the RADNEXT project [25]. Finally, the thermal neutron cross sections were measured at the D50 instrument of the Institut Laue-Langevin (ILL) nuclear reactor in France, providing a thermal neutron spectrum with a peak at 23 meV [21].

The setup for SEU measurements consists of a single SRAM (controlled through a motherboard) written with a checkboard pattern (consecutive 0–1) and read every 60 s. After each reading, the memory is written again with the initial pattern, and the SEE data are transferred to a laptop that controls the board via a graphical user interface. The SEU cross sections are calculated considering both single-bit upsets (SBUs) and multiple-bit upsets (MBUs), although MBUs were negligible. The SEL setup is instead composed of a board hosting either one or eight SRAMs, the latter configuration employed to increase the statistics when the beam sizes, flux, and homogeneity allow it. The current of the SRAMs is monitored via dedicated software controlling a power supply; once an SEL is detected, a power cycle is performed and the corresponding fluence, accounting for the hold and reset times, is not considered for the SEL cross section calculation.

The SRAMs were tested at room temperature and powered at 3.3 V at the memory (the voltage drop due to the cable length was taken into account) unless otherwise stated. When zero events are recorded, the SEE cross sections are calculated as upper limits according to a Poisson distribution.

III. SEU and SEL Response Functions—Experimental Observations

The experimental SEU and SEL cross sections of SRAM memories, which were extensively characterized in several facilities and environments [3], [5], [10], are presented in this section to compare their response as a function of the energy. Table I reports several SEE cross sections measured with high-energy protons (>180 MeV), 14-MeV neutrons, and the atmospheric spectra produced at ChipIr and TRIUMF. The SEE cross sections measured with atmospheric environments are computed using the integrated fluence above 10 MeV. The high-energy cross sections for the Alliance memory (SEL) increased up to a few GeV [26], and its value was simulated through FLUKA.

As introduced in Section I, above a few tens of MeV, the proton and neutron SEE cross sections can be assumed to be equal. Hence, the high-energy proton cross sections, utilized for characterizing components for accelerator applications or environments with hard spectra, are equivalent to the high-energy neutron cross sections. As a first observation, it is notable that even testing with an atmospheric spectrum (and considering the fluence above 10 MeV) underestimates the SEE cross sections at high energy, particularly for SEL, and hence the failure rate in environments with hard spectra (primarily the accelerator and avionics) [27]. In addition, the same components tested with the ChipIr and TRIUMF atmospheric spectra exhibit equivalent cross sections for SELs, while some more pronounced differences were observed in a few SEU-tested memories. The difference in the Integrated Silicon Solution, Inc. (ISSI) memory can be attributed to the fact that the spectrum at TRIUMF presents larger fluxes between 0.1 and 10 MeV, which will induce several SEUs, but the provided fluence considers only neutrons above 10 MeV. In addition, SEUs will also be induced by thermal neutrons, which are typically neglected in such facilities but are nevertheless present. Regarding the Cypress 90-nm memory, instead, it does not exhibit high sensitivity below 10 MeV [3], however, it was tested delidded (i.e., decapsulated) in ChipIr, which may explain the discrepancy observed, as noted also testing the same reference with 17-MeV neutrons in [3].

The SEE response as a function of the neutron energy of six relevant cases from Table I is depicted in Fig. 1, where

TABLE I

SEU AND SEL CROSS SECTIONS OF SEVERAL SRAMs, MEASURED WITH HIGH-ENERGY PROTONS LARGER THAN 180 MeV (σ_{HE}), 14-MeV NEUTRONS ($\sigma_{14\,\mathrm{MeV}}$), AND THE ATMOSPHERIC NEUTRON SPECTRA (FLUENCE > 10 MeV) AT CHIPIR (σ_{ChipIr}) AND TRIUMF (σ_{TRIUMF}). THE SEE CROSS SECTIONS ARE PRESENTED IN UNITS OF cm^2 AND TESTED AT 3.3 V (*5 V). (^{d}) DENOTES A DELIDDED MEMORY AND (^{s}) A SIMULATED VALUE

	SRAM memory	Reference	Size [Mbit]	Tech [nm]	σ_{HE} [cm^2]	σ_{14MeV} [cm^2]	σ_{ChipIr} [cm^2]	σ_{TRIUMF} [cm^2]	E_{th} [MeV]	W [MeV]	s
SEU	ISSI	IS61WV204816BLL-10TLI	32	40	$4.7\cdot10^{-7}$	$3.3\cdot10^{-7}$	$3.3\cdot10^{-7}$	$4.9\cdot10^{-7}$	0.01	14.05	0.82
	Cypress	CY62167GE30-45ZXI	16	65	$1.3\cdot10^{-6}$	$7.7\cdot10^{-7}$	$1.4\cdot10^{-6}$	$1.5\cdot10^{-6}$	0.01	11.57	0.80
	Cypress	CY62157EV30LL-45ZSXI	8	90	$1.8\cdot10^{-6}$	$4.2\cdot10^{-7}$	$^d4.8\cdot10^{-7}$	$1.3\cdot10^{-6}$	0.1	24.22	1.98
	ESA Mon.	AT68166H-YM20-E	16	250	$4.4\cdot10^{-7}$	$3.1\cdot10^{-7}$	$3.8\cdot10^{-7}$		0.2	13.8	2.99
SEL	Lyontek	LY62W20488ML-55LL	16	180	$*5.0\cdot10^{-8}$	$*4.8\cdot10^{-11}$		$1.3\cdot10^{-8}$	14	97.7	1.45
	ISSI	IS61LV5128AL-10TLI	4	180	$3.5\cdot10^{-8}$	$9.2\cdot10^{-13}$	$1.1\cdot10^{-8}$	$1.3\cdot10^{-8}$	14	168	1.41
	Brilliance	BS62LV1600EIP55	16	180	$2.6\cdot10^{-7}$	$2.0\cdot10^{-9}$	$1.0\cdot10^{-7}$	$1.4\cdot10^{-7}$	14	105	1.1
	Alliance	AS7C34098A-10TCN	4	200	$^s7.5\cdot10^{-9}$	$<2.8\cdot10^{-12}$	$7.1\cdot10^{-11}$		25	2210	1.41

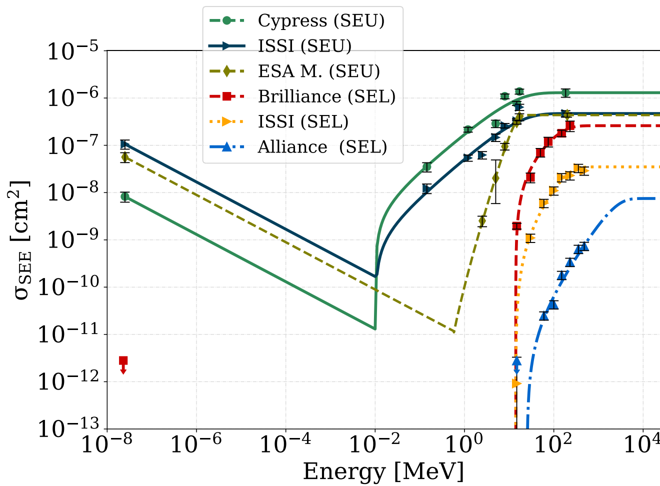

Fig. 1. SRAM SEU and SEL response as a function of the neutron energy calculated from experimental cross section measurements, which are shown as data points. The Cypress reference is based on 65-nm technology. The Brilliance SEL cross section measured with thermal neutrons and that of Alliance at 14 MeV are upper limits because no events were recorded. The ISSI memory measured only two SELs with 14-MeV neutrons. The cross sections are presented in units of [cm^2] to allow a direct comparison.

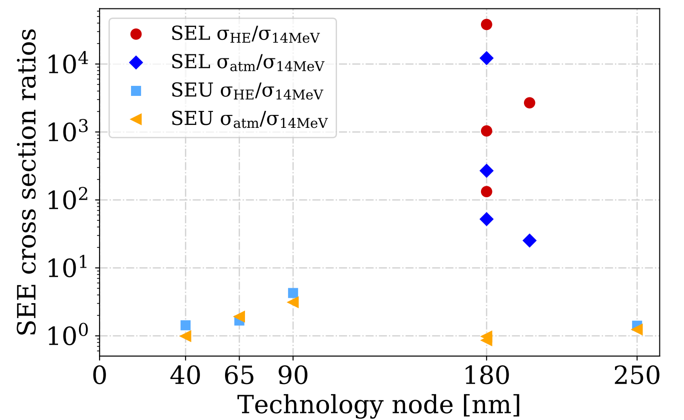

Fig. 2. Ratios between the SEE cross sections measured at high energies (with protons >180-MeV σ_{HE}, and with atmospheric neutrons σ_{atm}) and that measured with 14-MeV neutrons ($\sigma_{14\,\mathrm{MeV}}$), as a function of the technology node for the SRAMs from Table I. The SEU 180-nm cross sections are included from [11].

the experimental cross sections are fit with a Weibull function, whose parameters are reported in Table I. The experimental SEE cross sections were measured with protons for energies above 20 MeV and with neutrons for 14 MeV and below. The thermal neutron cross section (25 meV), which is attributable to the presence of ^{10}B contained inside the SRAMs, although free from borophosphosilicate glass (BPSG), is reported from [2] for the SEU-tested memories. The SEE cross section is extrapolated for the higher energies up to 0.01 MeV by scaling the thermal neutron cross section (σ_{ThN}) according to the $1/v$ law, where v is the neutron velocity. Indeed, the neutron absorption cross section of ^{10}B is inversely proportional to the neutron velocity, from thermal energies up to 0.01 MeV. As velocity and energy are correlated, the capture cross section $\sigma_c(E)$ can be calculated from the energy as $\sigma_c(E) = \sigma_{\mathrm{ThN}} \cdot \sqrt{(0.025/E[\mathrm{eV}])}$. In addition, the SEL thermal neutron cross section of the Brilliance memory, which showed the highest sensitivity to high-energy neutrons compared to other SEL-tested memories, was experimentally measured at ILL. Zero SELs were recorded, and hence, an upper limit value is reported in Fig. 1. Both SEU-tested memories present large sensitivity to neutrons between 0.01 and 10 MeV, while the SEL-tested memories represent the cases with low (Brilliance, ISSI) and high (Alliance) linear energy transfer (LET) onsets. The first graphical observation from the plot (and Table I) is that the relative SEL sensitivity is much lower than that of SEUs below ∼20 MeV. Specifically, the SEL cross section at 14 MeV is at least two orders of magnitude lower compared to the high-energy value, even considering the memory with larger sensitivity at this energy (Brilliance), while the ISSI and Alliance memories instead recorded only 2 and 0 SELs, respectively. At lower energies, only SEUs can be recorded and significant evidence of SELs is not observed in the literature.

The SEE high-energy cross sections (σ_{HE}, typically used in accelerator-oriented applications) and that measured with a spallation neutron source (σ_{atm}, relevant for atmospheric applications) are shown in relation to the cross section measured at 14 MeV in Fig. 2. The SEU $\sigma_{\mathrm{atm}}/\sigma_{14\,\mathrm{MeV}}$ ratios are close to one, in accordance to [11], and up to three for the Cypress 90-nm memory, while the SEL ratios are much larger up to several orders of magnitude. The 180-nm SEU data are included for the Lyontek LY62W20488ML-55LLI and the ISSI IS61LV5128AL-10TLI from [11]. Hence, for the

SRAM studied, 14 MeV, 180–200 MeV, and atmospheric neutrons yield compatible SEU cross sections, different from the SEL cross sections. As a result, 14-MeV neutrons can be employed as part of a cost-efficient screening procedure for components only against SEUs, and the physical reasons for this difference are elucidated in Sections IV and V.

IV. SEU and SEL Mechanisms—Inelastic Interactions Neutron–Silicon

In this study, natural silicon, composed of ^{28}Si (92.2%), ^{29}Si (4.7%), and ^{30}Si (3.1%), is considered as the primary element of interest constituting electronics. However, it should be noted that other materials are also utilized and may have an effect on the simulated SEE cross sections. When neutrons impact against silicon, secondary ions are generated through nuclear interactions. The incident neutron energy is the main parameter that determines the type of secondaries and their properties: relative production yields, range, LET, direction, and so on. Inelastic interactions (nuclear reactions), as opposed to elastic recoils, are the focus of the study, as the associated secondaries induce the majority of SEEs when the incident neutron energy is larger than roughly 5–10 MeV [3], [28], [29]. The average path traveled by neutrons before undergoing n-Si inelastic interactions (interaction length) is typically of the order of tens of cm (varying with the energy), which is substantially longer compared to typical sensitive volume (SV) sizes. Above roughly 100 MeV, the interaction length is 46 cm, and the probability of undergoing an inelastic interaction can be considered uniform. When the ionization charge released by these secondaries falls in the vicinity of an SRAM's node and is collected within the SV, if it exceeds a certain threshold defined as the critical charge (Q_c), an SEU is triggered. As will be discussed in Section V, more deposited energy is needed to trigger an SEL with respect to an SEU owing to the different mechanisms and its larger SVs (orders of magnitude). This aspect reflects the physical dimensions of the effects: an SEU involves well-defined p-n junctions of memory cells, whose volumes are smaller compared to those of an SEL, which comprises well, substrate, and drain–source contacts or even peripheral areas. In addition, also the timing characteristics substantially differ: for SEUs, only the prompt charge collection matters because the operation of the memory cell tends to remove the deposited charge, while for SELs, the charge can be collected along a larger volume and the timing depends on the specific configuration of the structure (such as the capacitance and parasitic resistance).

To understand the experimentally observed differences in the SEE cross sections, the simulations in this section are performed with FLUKA at the single interaction level (no transport) which relies on the Pre-Equilibrium Approach to NUclear Thermalization (PEANUT) model [30]. Fig. 3 shows the Z-distribution of the produced secondaries (in inelastic interactions) when incident neutrons of 14, 20, 100, and 200 MeV impact natural silicon. As can be seen, fragments induced by 14–20-MeV neutrons are either light (neutrons, H, and He) or relatively heavy (Mg, Al, and Si), while 100–200-MeV neutrons populate also the intermediate values ($2 < Z < 12$), although in a small percentage, and more He ions (mostly α) are produced. This phenomenon occurs because the open reaction channels with

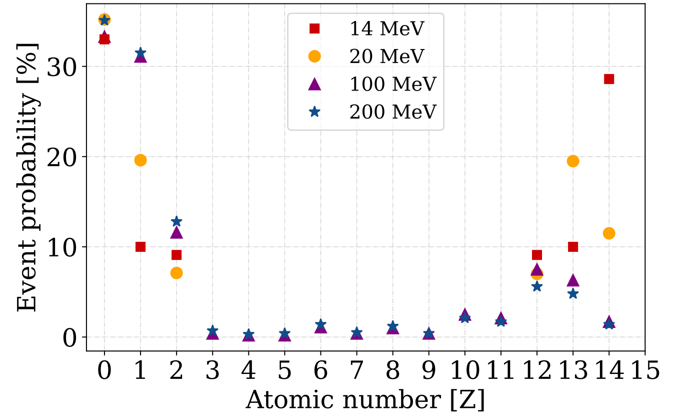

Fig. 3. Atomic number (Z) of the secondaries generated by the interaction of different incident neutron energies with natural silicon, simulated with FLUKA at the single interaction level. Secondary neutrons are shown at $Z = 0$. Notice that the yields for each energy are not absolute quantities.

TABLE II
Relative Yield (%) of the Most Probable Reactions Occurring With Incident Neutrons of 10, 14, 20, and 100 MeV in Natural Silicon

Reaction	10 MeV	14 MeV	20 MeV	100 MeV
Si(n,α)Mg	18.5	17.0	3.1	0.2
Si(n,α)Mg	0	2.1	15.3	2.1
Si(n,p)Al	17.9	17.4	5.9	1.4
Si(n,n)Si	62.8	55.8	25.5	2.7
Si(n,2n)Si	0.7	4.1	4.7	4.4
Si(n,np)Al	0	2.8	42.3	13.8
Si(n,d)Al	0	0.7	2.9	1.5
Total [%]	100	100	99.7	26.1

14- and 20-MeV neutrons are limited [31], as the neutron energy required to induce a nuclear reaction has to overcome a certain threshold, specific for each reaction. The higher the neutron energy, the more reaction channels become available as shown in Table II, simulated through FLUKA at the single interaction level, illustrating the relative yields of the most probable reactions occurring with incident neutrons of 10, 14, 20, and 100 MeV in natural silicon (with the latter energy also being representative of 200-MeV neutrons throughout this article). Reactions are reported in the form of target (projectile, products) residue, where the products can be alpha particles (α), protons (p), neutrons (n), and deuterons (d). As can be seen, these reactions cover almost 100% of the total reaction channels up to 20 MeV, while only 26% with 100-MeV neutrons. Notice that similar results from [11] using GEANT4 considering 14–200-MeV neutrons overestimate the Si production ($Z = 14$) and underestimate all other ions compared to the FLUKA simulations. For instance, the yield of alpha particles is very low, and fragments between $2 < Z < 7$ are absent in GEANT4 even with 200-MeV neutrons.

The respective LET distributions of secondaries produced by several incident neutrons are computed using FLUKA, with stopping and range of Ions in matter (SRIM) [32] employed for the energy-to-LET conversion. They are depicted in Fig. 4, showing the larger values obtained with 100-MeV neutrons (up to 14 $\mathrm{MeV \cdot cm^2/mg}$) compared to 14-MeV neutrons (up to 10 $\mathrm{MeV \cdot cm^2/mg}$).

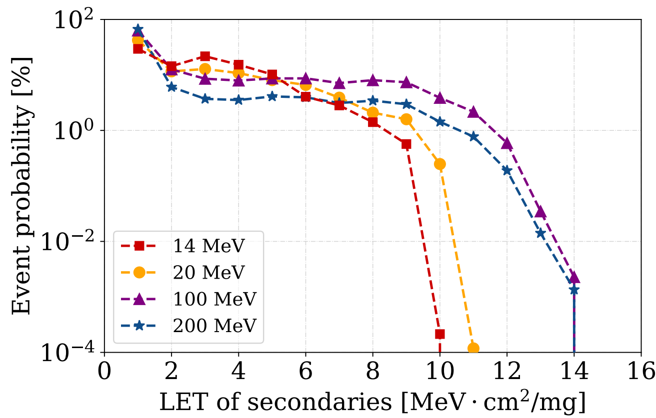

Fig. 4. LETs of secondaries generated by inelastic interaction considering different incident neutron energies in natural silicon, grouped in intervals of 1 MeV $\cdot$ cm^2/mg, whose energies are simulated with FLUKA at the single interaction level and converted to LET using SRIM.

However, the LET distributions are not sufficient to provide a comprehensive overview for the study, especially because they are similar below 6 MeV $\cdot$ cm^2/mg or even higher (He ions) in the 14-MeV case.

In fact, also the range of secondaries in relation to the SV dimensions and their energies are fundamental parameters, which, in turn, depend on the species of the secondary ions. The LET distributions with 14- and 100-MeV neutrons of Fig. 4 are broken down into the single-ion yield in Fig. 5, where ions falling within the range $2 < Z < 6$ are excluded due to their negligible impact. The larger LET values (7–10 MeV $\cdot$ cm^2/mg) are carried by Mg ($Z = 12$), while the lower LETs are dominated by Si and Al, and only below 1-MeV $\cdot$ cm^2/mg He and H ions are prevailing. With incident neutrons of 100 MeV, the larger LETs are carried by the heavier fragments (Si, Al, and Mg) and by the lighter ions (Na and Ne), the latter not produced with 14 MeV.

The energy transferred to the fragments with large LET is represented in the case of Mg in Fig. 6. As expected (and also observed for other ions), fragments from 100- and 200-MeV neutrons reach up to significantly larger energy than with 14 or 20 MeV, and hence have a longer range and higher LETs (because the Bragg's peak is on the right of the maximum fragment's energy). The longer range of these ions should be compared with the SV dimensions and therefore, it will not significantly affect a small volume (SEU), while for larger charge collection volumes (SEL), a fragment from 100 MeV will deposit several times more energy, as will be quantified in Section V. Notice that only a small fraction of the original neutron energy is transferred to the heavy fragments, while the energy transfer considerably increases with neutron energy for lighter ions (alpha particles have up to roughly 90% of the initial neutron energy). As a result, the energy deposition by 100-MeV neutrons with respect to 14 MeV in an SEL-like SV is expected to be larger than in an SEU volume: larger fragment energies lead to larger energy deposition in volumes comparable to their ranges. Furthermore, the probability of reaching the SV is also larger for SELs when secondaries are produced far from it.

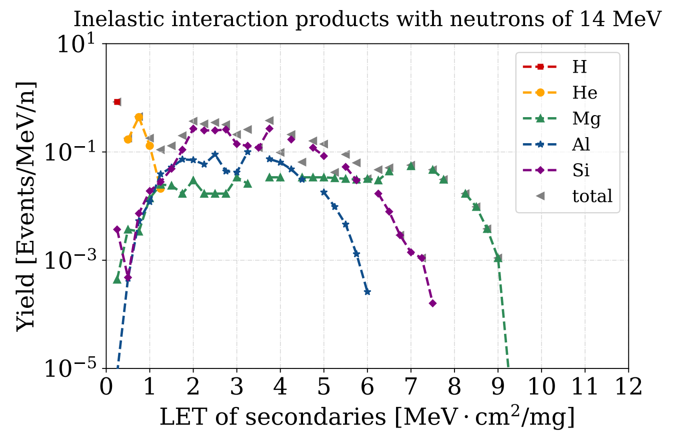

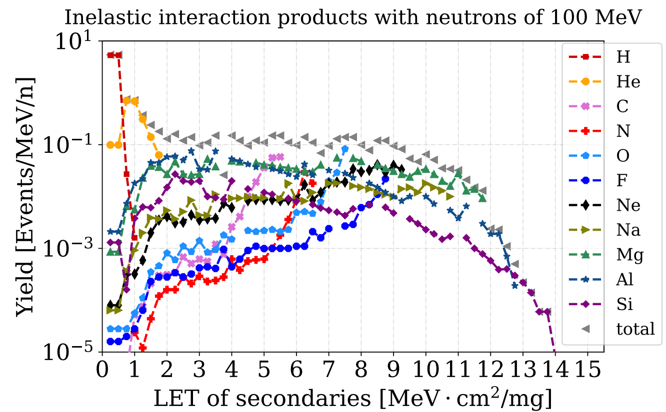

Fig. 5. Ions generated by the interaction of 14- and 100-MeV incident neutrons in natural silicon, simulated with FLUKA at the single interaction level. Ions between $2 < Z < 6$ produced with 100-MeV neutrons are neglected.

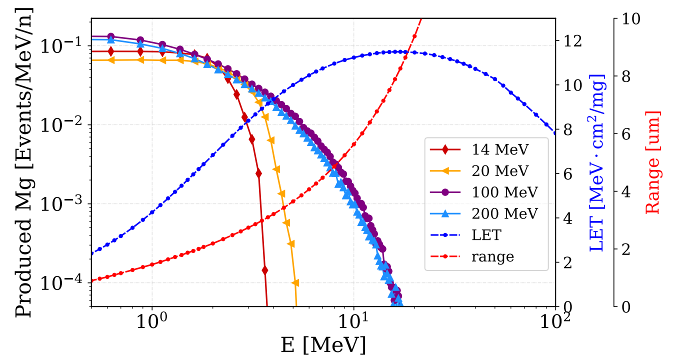

Fig. 6. Energy distribution of produced Mg ($Z = 12$) ions for several incident neutron energies. The LET and range are shown on the right axes, both extracted through SRIM.

V. Energy Deposition in SEU and SEL Sensitive Volumes and Cross Sections Calculation

Although the properties of the produced fragments from neutron–silicon interactions introduced in Section IV are highly relevant to evaluating the ionization mechanisms, the most representative quantity is the actual energy deposited in the SV. To this end, the event-by-event energy deposition is calculated through FLUKA inside volumes representative of the SEU and SEL mechanisms in SRAMs. The standard FLUKA Monte Carlo tool (v4-3.3) with the recently

TABLE III
GEOMETRIC PARAMETERS OF SEU AND SEL MODELS WHOSE SEE CROSS SECTIONS WERE BENCHMARKED EXPERIMENTALLY. Δ_z^{BEOL} AND Δ_z^{BULK} ARE THE THICKNESSES OF BEOL AND BULK, RESPECTIVELY

Model	Target [μm]				RPPs	SV [μm]		
	Δx	Δy	Δ_z^{BEOL}	Δ_z^{Bulk}		Δx	Δy	Δz
ISSI SEU	24.5	24.5	6	0.35	10x10	0.25	0.25	0.25
Brilliance SEL	249	89	7	30	10x10	20	4	3

introduced point-wise cross section card was employed (JEFF-3.3 library), as opposed to the production code used in Section IV, to simulate the energy deposition due to 14–200-MeV neutron elastic and inelastic interactions, although the former yields a minor SEE contribution. Table III reports the parameters of the ISSI (SEU) and Brilliance (SEL) models, which were selected to study also the thermal neutron sensitivity, as the former SRAM showed a large thermal neutron SEU cross section among tested memories. Instead, the latter presents one of the lowest SEL onset energies among tested memories, and hence, exhibits a large sensitivity at 14 MeV. In addition, the Brilliance memory was also measured against thermal neutrons (see Fig. 1). These SEE models are simplified geometries consisting of a silicon bulk containing the SV of the device, in which the energy deposition is calculated. These models aim to study how the energy is deposited in volumes resembling the SEU and SEL mechanisms rather than perfectly reproducing the measured SEE cross sections of the specific devices. The silicon target is large enough with respect to the SV to account for those ions with long-range (such as alpha particles) that can travel and deposit energy even far from the generation point. The SV is represented by a rectangular parallelepiped (RPP) located 6–7 μm deep in silicon to consider the back-end-of-line (BEOL), which is the latter stage of semiconductor device manufacturing, involving the interconnection and metallization of transistors and other components. To enhance the simulation time performance, multiple rectangular RPPs are considered instead of one, in a matrix of 10 × 10 units. BEOL, Bulk, and SV were all considered to be composed of silicon. While using an RPP for the SEU mechanism is common practice because the effect is localized within the memory cell, it represents a simplified model for SEL due to the different nature of the mechanism. An SEL involves a large volume, whose geometry may be different from that of an RPP as the charge can be collected along a long path and the collection efficiencies play an important role. Moreover, the angular dependence of the beam is not taken into account, which generally leads to a lower SEL cross section, and hence, considering a normal incidence beam tends to overestimate the SEL rate [33], [34], [35]. Other models have been proposed, for instance, using nested SVs [33] instead of a single RPP, which has been shown to better predict SEL cross sections at different angles. However, also this method relies on several assumptions (dimension and efficiencies of nested volumes) in addition to those already present with a single RPP. Given that this study aims to compare the energy deposition in volumes representative of SEU and SEL effects, the simplest model relying on a single RPP is chosen also for SELs, which was previously validated with protons [10], [26], neutrons [36], electrons [37], and pions [38].

Neutrons are simulated as a mono-directional beam traveling perpendicular to the SV thickness (the z-axis in Table III). The dimensions of the SEU volume are taken from [3] and [39] for the same memory, which is considered a cubic SV. The sizes of the SEL volume are assumed considering a cell size of 2×2 μm^2 from a very similar 180-μm reference [26], [40], and the fact that an SEL involves a surface of about 2×10 cells is based on laser studies from [41] and [42]. The typical dimensions of a single cell are also confirmed for this technology from the scanning electron microscopy (SEM) performed in several SRAMs in [43]. The thickness of the SEL volume is instead assumed to obtain the best fit with the experimental proton and neutron SEL cross sections.

The event-by-event energy deposition from incident neutrons is scored in the SVs by utilizing several FLUKA user routines described in [43]. The simulation output is a histogram of these events, where each bin represents the probability of depositing energy in the respective energy interval, which is associated with the probability of inducing an SEE. From the differential event-by-event energy deposition distribution $dN(E_d)/dE_d$, the SEE cross section for a given incident neutron energy can be calculated following two different approaches.

- *Fixed Critical Charge:* The SEE cross section is calculated by integrating the energy deposition events above a fixed critical energy through (1), where Φ is the simulated fluence retrieved as the inverse of the x–y simulated beam area (A_b). Notice that E_c can also be expressed in terms of Q_c through $E_d[\text{MeV}] = 22.5 \cdot Q_c[\text{pC}]$

$$\sigma_{\text{SEE}}(E_c) = \frac{1}{\Phi} \cdot \int_{E_c}^{+\infty} \frac{dN(E_d)}{dE_d} dE_d. \quad (1)$$

  In fact, if an SEE is triggered by a certain E_d, it will be triggered also by higher E_d. Noteworthy, this is a simplified method that assumes a step-like response. The critical charge defined for SEUs generally decreases with technology scaling, although it can assume a range of values in the order of a few fC for a single technology node due to its dependence on many parameters of the SRAM (node capacitance, internal voltages, etc.) [28], [44], [45]. Its value is typically calculated via a semi-empirical method, which provides the best SEU cross section fit with data measurements.
- *Ion Weibull Response:* The approach with a fixed Q_c assuming a step-like response is very simplistic and a more realistic response can be calculated by folding the event-by-event energy deposition distribution with the heavy-ion (HI) Weibull function [$w_{\text{HI}}(E_d)$] of the SRAM concerned. The formula is shown in the following equation, with $\sigma_{\text{HI}}^{\text{sat}}$ the HI cross section in saturation, A_{SV} the x–y surface of the SV and Φ the simulated fluence:

$$\sigma_{\text{SEE}} = \frac{\sigma_{\text{HI}}^{\text{sat}}}{\Phi \cdot A_{\text{SV}}} \cdot \int_{0}^{\infty} w_{\text{HI}}(E_d) \cdot \frac{dN(E_d)}{dE_d} E_d. \quad (2)$$

The HI Weibull function takes more realistically into account charge collection effects, for instance, the fact that events depositing more energy have a larger probability of triggering an SEE. However, the final SEE cross section

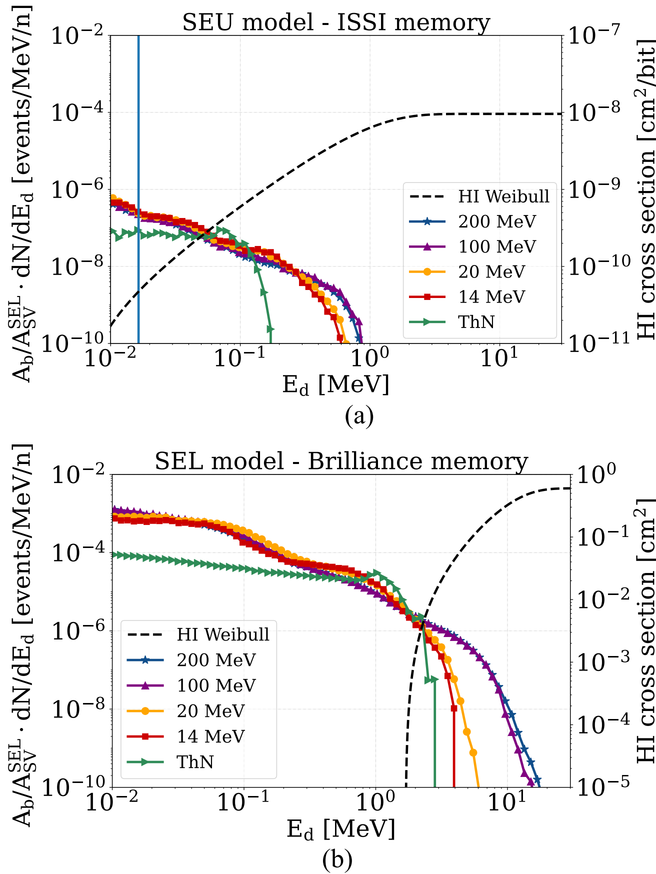

Fig. 7. FLUKA differential event-by-event energy deposition distributions for (a) SEU ISSI and (b) SEL Brilliance models, shown as a function of the deposited energy for several incident neutron energies including thermal neutrons. The events in both models are simulated using the same target irradiated area, which contains the respective SV. The HI Weibull function is included on the right axis and the SEU critical energy (0.016 MeV) corresponding to the critical charge of (0.73 fC) is shown with a vertical line.

strongly depends on the Weibull fit to the HI measurements, especially at energies around its threshold, when intersecting only with a few events.

Both methods can be applied for SEU models [46]. Concerning an SEL, instead, the charge collection efficiencies are more relevant with respect to those of an SEU, due to the larger SV sizes and different mechanisms, and using a single critical charge for SEL is too simplistic [47]. As initially shown in [48], the HI Weibull response fit with the energy deposition provides good agreement in predicting proton and neutron SEU and SEL cross sections, and this method was even employed by Airbus [11]. This approach for SEL was validated in several studies [10], [26], [36], [37], [38], and a similar method was used to predict SEU and SEL HI and proton rates in geostationary orbit by ESA [49]. Although an SEE depends on the collected charge and not only on the deposited charge, these models do not consider time windows within which the charge is collected.

A. Event-by-Event Energy Deposition From Neutrons

The differential event-by-event energy deposition distributions for the SEU and SEL models of Table III are shown in Fig. 7 as a function of E_d for several incident neutron energies including thermal neutrons. These event distributions are shown in [events/MeV/neutron] by irradiating the same target area, which contains a single SV. The target area is arbitrarily chosen to be 20 × 4 μm as the SEL SV surface (results would not change considering a bigger area). Therefore, a fraction of simulated neutrons will not pass through the SEU SV, as it is much smaller than the target area, but through the surrounding silicon target. In this way, the SEU and SEL energy deposition distributions can be directly compared. The SEE cross sections are calculated from the distributions of Fig. 7 through (2) and shown in Table IV. The conversion from LET (of the Weibull HI) to equivalent deposited energy E_d^{eq} can be calculated through the following equation, considering the silicon density $\rho = 2.33 \cdot 10^3$ mg/cm^3 and the assumed SV thickness SV_t:

$$E_d^{eq} = \text{LET} \cdot \rho \cdot SV_t \qquad [\text{MeV}]. \tag{3}$$

TABLE IV
SIMULATED SEU AND SEL CROSS SECTIONS

Model	σ_{14MeV} [cm^2]	σ_{100MeV} [cm^2]	σ_{200MeV} [cm^2]
SEU ISSI	$2.8 \cdot 10^{-7}$	$3.8 \cdot 10^{-7}$	$3.2 \cdot 10^{-7}$
SEL Brilliance	$7.0 \cdot 10^{-9}$	$1.6 \cdot 10^{-7}$	$1.7 \cdot 10^{-7}$

The simulations confirm that the SEU cross sections using incident neutrons of 14 and 100 MeV are almost the same (see Table IV), while the SEL cross sections differ by more than an order of magnitude. Compatible SEU cross sections are obtained by using a critical charge of 0.73 fC (0.016 MeV), according to previous works on the same ISSI memory [3], [39], while a single critical charge for SEL would not yield reliable results. Regardless, a range of critical charges can be calculated for SEL to fit the simulated cross sections with the measurements, resulting in 178 fC (4 MeV) and 251 fC (5.7 MeV) with 14- and 230-MeV neutrons, respectively.

Considering why 14- and 100-MeV neutrons yield a compatible SEU cross section (well representative of 200 MeV), while the same does not hold true for SELs, it is notable that the following holds.

- As can be seen in Fig. 7, the maximum energy deposited by neutrons in the SEL model is more than a factor of 10 larger with respect to that of the SEU model. In addition, the number of events for a given deposited energy is 3–4 orders of magnitude larger in the SEL model. These effects can be associated with the larger volume of an SEL, where more ions can interact and travel a longer path and hence have the possibility of depositing more energy.
- The critical charge for an SEU is relatively small and corresponds to the energy where the distribution of secondaries using either 14 or 100 MeV is essentially the same and constant [see Fig. 7(a)]. A small change in the critical charge will not significantly impact the final SEU cross section. As a result, secondaries from 14- and 100-MeV incident neutrons deposit essentially the same amount of energy in an SEU volume. This happens because fragments from 100 MeV release only a small fraction of their energy, primarily due to their long range, when compared to the SEU volume.

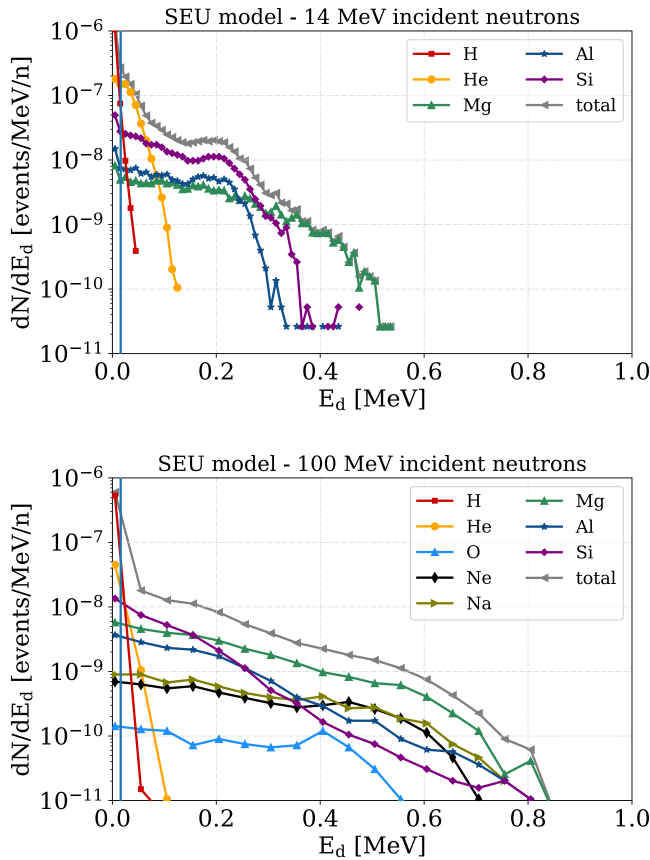

Fig. 8. G4SEE normalized event-by-event energy distribution of secondaries produced by the interaction of 14- (top) and 100-MeV (bottom) neutrons in an SV representative of the SEU mechanism.

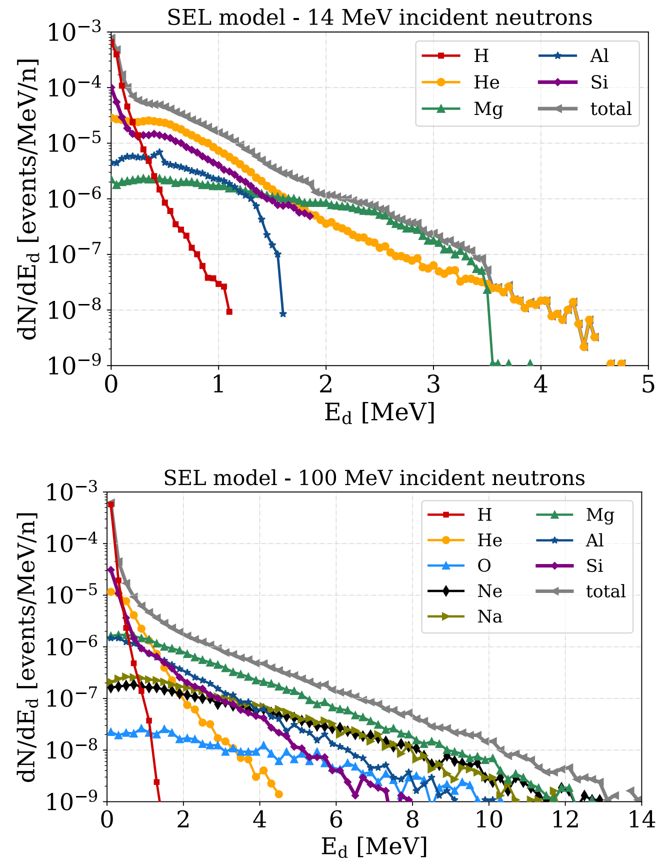

Fig. 9. G4SEE normalized event-by-event energy deposition of secondaries produced by the interaction of 14- (top) and 100-MeV (bottom) neutrons in an SV representative of the SEL mechanism.

- Contrary to this, the critical charge for an SEL, although as mentioned a single value is not representative for all energies, corresponds to a range of energies where the 14- and 100-MeV distributions [see Fig. 7(b)] are significantly different (above ∼2 MeV), with a notable decrease of E_d and events induced by 14 MeV. The energy deposited by the produced fragments is large enough to trigger an SEL only with 100-MeV neutrons, as their range is compatible with the volume susceptible to SEL.

Furthermore, to disentangle the contribution of individual ions to the deposited energy needed to trigger an SEE by 14- and 100-MeV neutrons, Figs. 8 and 9 show the differential yield distributions for the SEU and SEL models simulated with G4SEE [16], respectively. The final yields to the SEU and SEL cross sections are shown in Table V for each ion, by integrating these energy distributions above the critical energies (calculated above). It is evident that any species of secondaries with energy deposition above the critical threshold of 0.016 MeV (as calculated earlier and illustrated in Fig. 8 by a vertical line) will trigger an SEU. For SEUs, at both incident neutron energies, the predominant contributors are Si, Al, Mg, and He ions.

Instead, given that the critical energies for an SEL are much larger (varying between 4 and 5.7 MeV), only a minimal fraction of the produced alpha particles will induce SEL at 14 MeV, while their contribution is negligible at 100 MeV, where instead the heavier Mg, Ne, and Na ions are prevailing. Remarkably, the impact of Si and Al ions is significant for SEUs but negligible for SELs when using both 14- and 100-MeV neutrons. These results were not evident through standard examination of produced secondaries from neutron–silicon interactions, such as LET, energy, and range (see Section IV). Instead, they required a detailed analysis of the deposited energy by secondaries in compatible SEE volumes. It is essential to note that this analysis is conducted solely with silicon as a target. The distributions of secondary ions change when a more detailed geometry is considered; for instance, when introducing a BEOL of SiO_2, a high yield of O and C ions is produced in the event-by-event energy deposition distributions.

TABLE V

Contribution of Secondary Ions (in Percentage), Produced by 14- and 100-MeV Incident Neutrons, to the Energy Deposition Accountable for the SEU and SEL Cross Sections

SEE	E_n [MeV]	Si	Al	Mg	Na	Ne	O	He	H
SEU	14	38	15	14	0	0	0	32	0
	100	30	16	31	7	6	1	10	0
SEL	14	0	0	0	0	0	0	100	0
	100	2	7	46	19	22	4	0	0

B. SEU and SEL Cross Sections With Thermal Neutrons

Thermal neutrons are captured by the ^{10}B isotope (relative abundance of 19.9%), inducing one of the two following reactions:

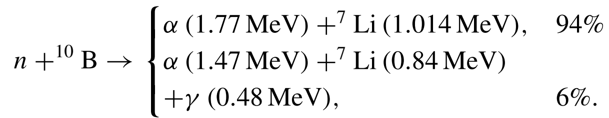

$$n + ^{10}\mathrm{B} \rightarrow \begin{cases} \alpha\,(1.77\,\mathrm{MeV}) + ^{7}\mathrm{Li}\,(1.014\,\mathrm{MeV}), & 94\% \\ \alpha\,(1.47\,\mathrm{MeV}) + ^{7}\mathrm{Li}\,(0.84\,\mathrm{MeV}) & \\ +\gamma\,(0.48\,\mathrm{MeV}), & 6\%. \end{cases}$$

Neglecting losses, the produced ions (α, ^{7}Li) can release a maximum combined energy of either 2.78 (ground state, 94% of the times) or 2.31 MeV (exited state, 6% of the times) in an SV. However, this occurrence in an SV is very rare due to the distinct ranges, LET, and directions of the products [31]. Their maximum ranges in Si are 5–9 μm; hence, only boron located within such distances from the SV is of interest.

The thermal neutron cross sections were simulated using the SEU and SEL models, considering the silicon bulk with a uniform concentration of natural boron, and the event-by-event energy distributions are shown in Fig. 7. These events are induced by the interaction of ^{10}B with thermal neutrons, as no energy deposition occurs if boron is not introduced in the simulation models. The SEU thermal neutron cross section of the ISSI memory was simulated to match the experimental value of $3.16 \cdot 10^{-15}$ cm^2/bit ($1.1 \cdot 10^{-7}$ cm^2) obtained through measurements [2], by using a boron concentration of $6.5 \cdot 10^{19}$ atoms/cm^3, and hence a ^{10}B concentration of $1.3 \cdot 10^{19}$ cm^{-3}. For comparison, the secondary ion mass spectrometry (SIMS) analysis on a 45-nm SRAM from [50] measured a ^{10}B concentration value of $2.0 \cdot 10^{20}$ cm^{-3}. However, the referenced study measured a Si concentration inside the SRAM of $1.0 \cdot 10^{21}$ cm^{-3}, instead of the standard value of $5.0 \cdot 10^{22}$ cm^{-3}.

Regarding the SEL sensitivity to thermal neutrons, given that no SELs were experimentally recorded with the Brilliance memory and no evidence is found in the literature, the high concentration found in the ISSI memory (SEU) was introduced in the SEL model as a worst case scenario. The energy deposition events are shown in Fig. 7(b), and (2) yields a thermal neutron cross section of $3.3 \cdot 10^{-9}$ cm^2, which is still nearly two orders of magnitude lower than the high-energy cross section. This result strongly depends on the onset LET of the Weibull function, and as shown in Fig. 7(b), the product $w_{\mathrm{HI}}(E_d) \cdot dN(E_d)/dE_d$ from (2) is not zero only for a few events. As a conclusion, and recalling the fact that the Brilliance memory has a low-onset threshold relative to other memories, thermal neutrons are unlikely to induce SELs also from a simulation point of view. However, SEL devices with low-LET onsets (roughly below 2 MeV $\cdot$ cm^2/mg) could be sensitive to thermal neutrons.

VI. Conclusion

The study presented in this article employs Monte Carlo simulations to explain the experimental differences observed in the SEU and SEL cross sections when testing SRAMs with 14-MeV neutrons and high-energy beams (>100 MeV). We illustrate the reason why the SEL cross sections at 14-MeV neutrons are more than two orders of magnitude lower than the high-energy values, while the SEU cross sections remain almost the same. The properties of the secondary products from neutron–silicon interactions are analyzed, which are relevant for understanding ionization mechanisms. However, only the analysis of the event-by-event energy deposition in volumes resembling the actual devices can explain how the energy is released and which ions contribute to triggering SEEs.

To induce an SEL, the produced secondaries need to deposit larger energies than for an SEU, which is provided only with 100-MeV (or equivalently 200 MeV) neutrons by Mg, Ne, and Na ions, not present with neutrons of 14–20 MeV. This fact is associated with the dimensions of the respective SVs, significantly larger for the SEL mechanism. Notably, alpha particles contribute solely to the relatively low SEL cross section with 14 MeV, becoming a negligible contribution with 100-MeV neutrons. Hence, fragments with a long-range release more energy due to the larger track length and the higher probability of reaching the volume when produced outside of it.

Differently, in an SEU volume, these ions release only a small fraction of their energy due to their long-range compared to the SV sizes, and the critical energy to trigger an SEU is already reached with fragments induced by 14-MeV neutrons. Consequently, the lower LET ions such as alpha particles yield a substantial contribution to the SEU cross section (while almost absent in that for SEL) along with Si, Mg, and Al ions. It is worth recalling that testing SEUs with 14-MeV neutrons instead of high-energy beams is an alternative applicable for non-critical systems, given the possible underestimation of both MCUs and SEU cross sections for components presenting high-Z materials.

In addition, the SEU thermal neutron cross section experimentally measured was simulated with the same model considering a boron concentration of $6.5 \cdot 10^{19}$ atoms/cm^3 for a 40-nm SRAM. The SEL sensitivity to thermal neutrons was also investigated demonstrating its very small probability of occurrence, owing to the low deposited energies of the alpha and ^{7}Li products. However, devices with LET thresholds lower than roughly 2 MeV $\cdot$ cm^2/mg may result in non-negligible SEL sensitivity to thermal neutrons.

References

[1] *Measurement and Reporting of Alpha Particle and Terrestrial Cosmic Ray-Induced Soft Errors in Semiconductor Devices*, Standard JEDEC JESD89B, Sep. 2021.

[2] M. Cecchetto et al., "Thermal neutron-induced SEUs in the LHC accelerator environment," *IEEE Trans. Nucl. Sci.*, vol. 67, no. 7, pp. 1412–1420, Jul. 2020.

[3] M. Cecchetto et al., "0.1–10 MeV neutron soft error rate in accelerator and atmospheric environments," *IEEE Trans. Nucl. Sci.*, vol. 68, no. 5, pp. 873–883, May 2021.

[4] R. G. Alía et al., "Single event effects in high-energy accelerators," *Semicond. Sci. Technol.*, vol. 32, no. 3, Feb. 2017, Art. no. 034003.

[5] M. Cecchetto, R. G. Alía, S. Gerardin, M. Brugger, A. Infantino, and S. Danzeca, "Impact of thermal and intermediate energy neutrons on SRAM SEE rates in the LHC accelerator," *IEEE Trans. Nucl. Sci.*, vol. 65, no. 8, pp. 1800–1806, Aug. 2018.

[6] K. Roed et al., "FLUKA simulations for SEE studies of critical LHC underground areas," *IEEE Trans. Nucl. Sci.*, vol. 58, no. 3, pp. 932–938, Jun. 2011.

[7] D. Lambert, F. Desnoyers, and D. Thouvenot, "Investigation of neutron and proton SEU cross-sections on SRAMs between a few MeV and 50 MeV," in *Proc. Eur. Conf. Radiat. Effects Compon. Syst.*, Sep. 2009, pp. 148–154.

[8] R. G. Alía, M. Brugger, S. Danzeca, J. Mekki, and A. Thornton, "SEE cross section calibration and application to quasi-monoenergetic and spallation facilities," *EPJ Web Conf.*, vol. 153, Sep. 2017, Art. no. 08015, doi: 10.1051/epjconf/201715308015.

[9] D. Lambert et al., "Analysis of quasi-monoenergetic neutron and proton SEU cross sections for terrestrial applications," *IEEE Trans. Nucl. Sci.*, vol. 53, no. 4, pp. 1890–1896, Aug. 2006.

[10] R. G. Alía et al., "SEL cross section energy dependence impact on the high energy accelerator failure rate," *IEEE Trans. Nucl. Sci.*, vol. 61, no. 6, pp. 2936–2944, Oct. 2014.

[11] C. Weulersee et al., "Preliminary guidelines and predictions for 14-MeV neutron SEE testing," *IEEE Trans. Nucl. Sci.*, vol. 64, no. 8, pp. 2268–2275, Aug. 2017.

[12] *FLUKA Toolkit*. Accessed: Jan. 2023. [Online]. Available: https://fluka.cern

[13] G. Battistoni et al., "Overview of the FLUKA code," *Ann. Nucl. Energy*, vol. 82, pp. 10–18, Aug. 2015.

[14] V. Vlachoudis, "FLAIR: A powerful but user friendly graphical interface for FLUKA," in *Proc. Int. Conf. Math., Comput. Methods React. Phys. (MC)*, Saratoga Springs, NY, USA, 2009, pp. 790–800.

[15] C. Ahdida et al., "New capabilities of the FLUKA multi-purpose code," *Frontiers Phys.*, vol. 9, Jan. 2022, Art. no. 788253.

[16] D. Lucsanyi, R. G. Alia, K. Bilko, M. Cecchetto, S. Fiore, and E. Pirovano, "G4SEE: A Geant4-based single event effect simulation toolkit and its validation through monoenergetic neutron measurements," *IEEE Trans. Nucl. Sci.*, vol. 69, no. 3, pp. 273–281, Mar. 2022.

[17] C. Weulersee et al., "Contribution of thermal neutrons to soft error rate," *IEEE Trans. Nucl. Sci.*, vol. 65, no. 8, pp. 1851–1857, Aug. 2018.

[18] M. Dentan et al., "Preliminary study of electronics reliability in ITER neutron environment," in *Proc. 22nd Eur. Conf. Radiat. Effects Compon. Syst. (RADECS)*, Venice, Italy, Oct. 2022, pp. 1–5.

[19] W. Hajdas, F. Burri, C. Eggel, R. Harboe-Sorensen, and R. de Marino, "Radiation effects testing facilities in PSI during implementation of the proscan project," in *Proc. IEEE Radiat. Effects Data Workshop*, Jul. 2002, pp. 114–118.

[20] E. R. van der Graaf, R. W. Ostendorf, M.-J. van Goethem, H. H. Kiewiet, M. A. Hofstee, and S. Brandenburg, "AGORFIRM, the AGOR facility for irradiations of materials," in *Proc. Eur. Conf. Radiat. Effects Compon. Syst.*, Sep. 2009, pp. 451–454.

[21] J. Beaucour et al., "Grenoble large scale facilities for advanced characterisation of microelectronics devices," in *Proc. 15th Eur. Conf. Radiat. Effects Compon. Syst. (RADECS)*, Moscow, Russia, Sep. 2015, pp. 312–315.

[22] A. Pietropaolo et al., "The Frascati neutron generator: A multipurpose facility for physics and engineering," *J. Phys., Conf.*, vol. 1021, May 2018, Art. no. 012004, doi: 10.1088/1742-6596/1021/1/012004.

[23] D. Chiesa et al., "Measurement of the neutron flux at spallation sources using multi-foil activation," *Nucl. Instrum. Methods Phys. Res. A, Accel. Spectrom. Detect. Assoc. Equip.*, vol. 902, pp. 14–24, Sep. 2018. [Online]. Available: http://www.sciencedirect.com/science/article/pii/S016890021830737X

[24] E. W. Blackmore, P. E. Dodd, and M. R. Shaneyfelt, "Improved capabilities for proton and neutron irradiations at TRIUMF," in *Proc. IEEE Radiat. Effects Data Workshop*, Jan. 2003, pp. 149–155.

[25] R. G. Alía et al., "Heavy ion energy deposition and SEE intercomparison within the RADNEXT irradiation facility network," *IEEE Trans. Nucl. Sci.*, vol. 70, no. 8, pp. 1596–1605, Mar. 2023.

[26] R. G. Alía et al., "Energy dependence of tungsten-dominated SEL cross sections," *IEEE Trans. Nucl. Sci.*, vol. 61, no. 5, pp. 2718–2726, Oct. 2014.

[27] M. Cecchetto, R. García Alía, and F. Wrobel, "Impact of energy dependence on ground level and avionic SEE rate prediction when applying standard test procedures," *Aerospace*, vol. 6, no. 11, Nov. 2019, Art. no. 119.

[28] S.-I. Abe and Y. Watanabe, "Analysis of charge deposition and collection caused by low energy neutrons in a 25-nm bulk CMOS technology," *IEEE Trans. Nucl. Sci.*, vol. 61, no. 6, pp. 3519–3526, Dec. 2014.

[29] B. D. Sierawski et al., "Contribution of low-energy (< 10 MeV) neutrons to upset rate in a 65 nm SRAM," in *Proc. IEEE Int. Rel. Phys. Symp.*, May 2010, pp. 395–399.

[30] A. Ferrari and P. Sala, "The physics of high energy reactions," in *Proc. Workshop Nucl. Reaction Data Nucl. Reactors Phys., Design Saf.*, Dec. 1998, p. 424.

[31] F. Wrobel, J.-M. Palau, M. C. Calvet, O. Bersillon, and H. Duarte, "Incidence of multi-particle events on soft error rates caused by n-Si nuclear reactions," *IEEE Trans. Nucl. Sci.*, vol. 47, no. 6, pp. 2580–2585, Dec. 2000.

[32] J. F. Ziegler, M. D. Ziegler, and J. P. Biersack, "SRIM—The stopping and range of ions in matter (2010)," *Nucl. Instrum. Methods Phys. Res. Sect. B, Beam Interact. Mater. At.*, vol. 268, nos. 11–12, pp. 1818–1823, Jun. 2010. [Online]. Available: http://www.sciencedirect.com/science/article/pii/S0168583X10001862

[33] P. Wang et al., "Sensitive-volume model of single-event latchup for a 180-nm SRAM test structure," *IEEE Trans. Nucl. Sci.*, vol. 67, no. 9, pp. 2015–2020, Sep. 2020.

[34] L. Artola et al., "Analysis of angular dependence of single-event latchup sensitivity for heavy-ion irradiations of 0.18-μm CMOS technology," *IEEE Trans. Nucl. Sci.*, vol. 62, no. 6, pp. 2539–2546, Dec. 2015.

[35] J. M. Hutson et al., "The effects of angle of incidence and temperature on latchup in 65 nm technology," *IEEE Trans. Nucl. Sci.*, vol. 54, no. 6, pp. 2541–2546, Dec. 2007.

[36] M. Cecchetto et al., "SEE flux and spectral hardness calibration of neutron spallation and mixed-field facilities," *IEEE Trans. Nucl. Sci.*, vol. 66, no. 7, pp. 1532–1540, Jul. 2019.

[37] M. Tali et al., "Mechanisms of electron-induced single-event latchup," *IEEE Trans. Nucl. Sci.*, vol. 66, no. 1, pp. 437–443, Jan. 2019.

[38] A. Coronetti et al., "The pion single-event effect resonance and its impact in an accelerator environment," *IEEE Trans. Nucl. Sci.*, vol. 67, no. 7, pp. 1606–1613, Jul. 2020.

[39] R. G. Alía et al., "Direct ionization impact on accelerator mixed-field soft-error rate," *IEEE Trans. Nucl. Sci.*, vol. 67, no. 1, pp. 345–352, Jan. 2020.

[40] A. J. Burnell, A. M. Chugg, and R. Harboe-Sørensen, "Laser SEL sensitivity mapping of SRAM cells," *IEEE Trans. Nucl. Sci.*, vol. 57, no. 4, pp. 1973–1977, Aug. 2010.

[41] N. A. Dodds et al., "SEL-sensitive area mapping and the effects of reflection and diffraction from metal lines on laser SEE testing," *IEEE Trans. Nucl. Sci.*, vol. 60, no. 4, pp. 2550–2558, Aug. 2013.

[42] E. Faraud et al., "Investigation on the SEL sensitive depth of an SRAM using linear and two-photon absorption laser testing," *IEEE Trans. Nucl. Sci.*, vol. 58, no. 6, pp. 2637–2643, Dec. 2011.

[43] R. G. Alia, "Radiation fields in high energy accelerators and their impact on single event effects," Ph.D. dissertation, Dept. Inf. IS, Montpellier Univ., Montpellier, France, 2014.

[44] R. Naseer, Y. Boulghassoul, J. Draper, S. DasGupta, and A. Witulski, "Critical charge characterization for soft error rate modeling in 90 nm SRAM," in *Proc. IEEE Int. Symp. Circuits Syst. (ISCAS)*, May 2007, pp. 1879–1882.

[45] D. Kobayashi, "Scaling trends of digital single-event effects: A survey of SEU and SET parameters and comparison with transistor performance," *IEEE Trans. Nucl. Sci.*, vol. 68, no. 2, pp. 124–148, Feb. 2021.

[46] M. Huhtinen and F. Faccio, "Computational method to estimate single event upset rates in an accelerator environment," *Nucl. Instrum. Methods Phys. Res. A, Accel. Spectrom. Detect. Assoc. Equip.*, vol. 450, no. 1, pp. 155–172, Aug. 2000.

[47] S. Guagliardo et al., "Single-event latchup sensitivity: Temperature effects and the role of the collected charge," *Microelectron. Rel.*, vol. 119, Apr. 2021, Art. no. 114087. [Online]. Available: https://www.sciencedirect.com/science/article/pii/S0026271421000536

[48] E. Normand, "Extensions of the burst generation rate method for wider application to proton/neutron-induced single event effects," *IEEE Trans. Nucl. Sci.*, vol. 45, no. 6, pp. 2904–2914, Dec. 1998.

[49] M. Pinto et al., "Parametric evaluation of the SEE rate on the SEU and SEL monitors aboard the alphasat using the IRPP model," *IEEE Trans. Nucl. Sci.*, vol. 70, no. 8, pp. 1821–1828, Aug. 2023.

[50] S.-J. Wen, S. Y. Pai, R. Wong, M. Romain, and N. Tam, "B10 finding and correlation to thermal neutron soft error rate sensitivity for SRAMs in the sub-micron technology," in *Proc. IEEE Int. Integr. Rel. Workshop Final Rep.*, Oct. 2010, pp. 31–33.